

# Seismic Site Response of A Large Deep-seated Rock Slope Revealed by Field Monitoring and Geophysical Methods

Hui Wang

State Key Laboratory of Geohazard Prevention and Geoenvironment Protection

Shenghua Cui (✉ [shenghuacui.geo@gmail.com](mailto:shenghuacui.geo@gmail.com))

State Key Laboratory of Geohazard Prevention and Geoenvironment Protection

Xiangjun Pei

State Key Laboratory of Geohazard Prevention and Geoenvironment Protection

Ling Zhu

State Key Laboratory of Geohazard Prevention and Geoenvironment Protection

Qingwen Yang

State Key Laboratory of Geohazard Prevention and Geoenvironment Protection

Runqiu Huang

State Key Laboratory of Geohazard Prevention and Geoenvironment Protection

---

## Research Article

**Keywords:** Rock slope, Seismic response, Peak acceleration, HVSR, Long-term seismic monitoring, Geological condition influence

**Posted Date:** September 28th, 2021

**DOI:** <https://doi.org/10.21203/rs.3.rs-916217/v1>

**License:** © ⓘ This work is licensed under a Creative Commons Attribution 4.0 International License.

[Read Full License](#)

---

# Abstract

Shidaguan Slope (hereinafter short for SDG Slope) is an unstable rock slope with an area of  $30.78 \times 10^4$  m<sup>2</sup> and a deformation depth of 30-70 m in Maoxian County, Sichuan Province, China. Three seismometers (P2-P4) with high sensitivity were installed at different locations on the unstable part of the slope. P2 and P3 were almost at the same elevation (2221 m and 2247 m), while P4 was the lowest (at 2140 m). Another seismometer (P1) sat in a stable location at a higher elevation (2373 m). 99 shallow earthquakes were analyzed. According to the peak acceleration ratios of three seismometers (P2-P4) on the unstable part and another seismometer (P1) on the stable part, the points at lower elevations showed greater seismic amplification (with the amplification coefficient of 2.64-3.51) than one at a higher elevation. And points at relatively thinner part (23 m thick) of unstable slope showed greater seismic amplification than ones at thick part (60-75 m thick). The same rule was also found in studying the site-epicenter azimuth and earthquake magnitude data. Based on the relationship between amplification coefficient and resistivity and rock core, the seismic response amplification was affected by the lithofacies difference. The lithofacies with resistivity values of 50-100 Ohm.m and RQD values of 0-50 % incurred seismic response amplification, which was restrained by the below lithofacies with resistivity values of 10-50 Ohm.m and ROD values of 0 %. When building on slope areas, the lithofacies difference should be taken into full consideration.

## 1. Introduction

Researchers had realized a few decades ago that topography made difference to the seismic amplification effect. For example, Leonov (1960) found during a Ms 7.4 earthquake that the topographic amplification effect at the top of slopes gave rise to many co-seismic landslides on top of ridges. Later, more and more researchers combined topography with the seismic amplification effect together. A lot of researchers suggest that obvious topographic amplification effects usually happen on the top of mountain slopes, ridges, and hills (e.g., Boore 1972; Celebi 1987; Huang and Chiu 1999; Lee et al. 2009). Boore (1972) and Bouchon (1973) also found that seismic response showed abnormal amplification at high elevation when slope base width was similar to wavelength. By analyzing the monitoring data of over 40 aftershocks obtained by Wang et al. (2012) through monitoring, it was concluded that seismic response became more intensive while getting closer to free face, showing the non-linear change of increasing gradually from inside to outside of the slope. Shen et al. (2019) found by monitoring the aftershocks of the Jiuzhaigou Earthquake that isolated protruding mountains reflected more intensive seismic response.

Some recent researches indicate that geology is also an influencing factor of ground motion amplification. Wang et al. (2012) and Ma et al. (2019) discovered that extreme amplification of seismic response would happen to overburdens and landslide deposits. Based on the seismic data obtained by Danneels et al. (2008) through field monitoring, the thicker overburdens showed a greater amplification effect than thinner ones. Kleinbrod et al. (2017) concluded by measuring the ambient noise that unstable part of rock slope revealed a more intensive seismic amplification effect than the stable part. Song et al.

(2020)'s finite element numerical simulation analysis results suggested that seismic waves would have numerous reflection and refraction at joint faces and amplify around the discontinuities on top of the slope. However, there are few kinds of research on how does geological conditions affect the seismic response of a large-scale deep-seated unstable slope. We have set four seismometers on the SDG Slope in this paper and have made seismic monitoring for nearly two years to get the ground motion amplification of the unstable slope area and stable slope area in different elevations. Furthermore, we studied geological conditions through geophysical measurement, for 1) analyzing amplification characteristics of rock slope in different positions, and 2) explaining the amplification phenomenon with slope geological characteristics.

## 2. Sdg Unstable Rock Slope

Figure 1a reveals the epicenter distribution situation of historical earthquakes that have happened around the study area since 1990. According to the result, the neotectonic movement was relatively intensive, earthquakes often happened. The epicenters of historical earthquakes that happened since 1990 were mainly distributed in the southeast part of the study area. The study area has experienced a total of 3466 earthquakes in Ms 3.5-5.0 since 1990 according to Fig. 1b. In addition to the 434 Ms 5.1-7.0 earthquakes, the study area has mainly suffered from the Ms 7.5 Diexi Earthquake, Ms 7.2 Songpan-Pingwu Earthquake, Ms 8.0 Wenchuan Earthquake, and Ms 7.0 Jiuzhaigou Earthquake in succession.

The study area (Fig. 2) involves tectonic-eroded Zhongshan River Valley geomorphology. The elevation difference between the Valley to the back edge of the unstable slope is 2450 m. The average gradient of the section from the Valley to the place at an elevation of 2000 m is 70°. The average gradient of the section from the place at an elevation of 2000 m to the peak of the unstable slope is 25°. And the average gradient of the stable slope on the upper part of the unstable slope is 50°. The outcrops of the study area are mainly composed of phyllite in the Upper Formation of Devonian Weiguan Group, Quaternary landslide deposits, Quaternary pluvial alluvial deposits, and Quaternary colluvial deposits.

The rear edge of SDG Unstable Slope is the back scarp of the deep and large tension crack developed by the sliding. The shear outlet on the front edge is at an altitude of 2000 m. The deformed body covers an area of  $30.78 \times 10^4 \text{ m}^2$  with an average longitudinal length of 540 m and an average width of 560 m. The slope showed signs of deformation since 2013. In 2014, a collapse with a height of 200 m appeared in the middle of the front edge. Nearly  $6 \times 10^4 \text{ m}^3$  deposits rushed into Minjiang River and developed into congestion taking up nearly 1/3 of the river channel. Meanwhile, the rear edge of the unstable slope started to crack. The deformation situation obviously got worse in 2015 and wider and wider cracks occurred. The slope deformation progress continued in 2016 and suddenly slowed down in July 2017 after some parts of the rear edge and front edge shifted down by more than 10 m.

## 3. Seismic Monitoring And Seismic Events

Seismometers were placed on the 40 cm-deep cement base. Each seismometer was equipped with a high-sensitivity three-component seismic sensor with a sensitivity of  $1.2722 \times 10^{10}$  cnt/m/s. The seismometers can collect components of seismic waves in three directions (horizontal EW direction, horizontal SN direction, and vertical direction) and record data unremittingly for 24 h at the sampling rate of 200 Hz. Four seismometers in total were set at different locations. Station P1 was set outside the rear edge boundary of SDG Unstable Slope, at the elevation of 2373 m, which was the highest. Station P2 was set beside the left boundary of the unstable slope at the elevation of 2221 m, in which the most significant deformation was developed. Station P3 and Station P4 were located in the middle and lower part of the unstable slope at the elevations of 2247 m and 2140 m, respectively. Refer to Fig. 3 for the distribution of monitoring stations on SDG Slope.

Seismic data studied in this paper are three-component data in MSD format. EW, NS, and Z respectively represent the horizontal east-west direction, horizontal south-north direction, and vertical direction. The four seismometers in the study area unremittingly recorded seismic data from July 17th, 2019 to March 21st, 2021. According to the earthquake catalog released by China Earthquake Network Center (CENC), corresponding seismic data were selected out from monitoring data as the research basis in this paper. 99 groups of seismic data with clear seismic waves had been selected in this paper. Figures 4a and 4c show the relative position of collected earthquake epicenters to SDG Slope, and Fig. 4b shows the earthquake magnitude ranging from 3.0 to 5.7. The epicenter distance ranged from 28 to 420 km and the hypocenter depth ranged from 2 to 40 km. These data have given great support to study the seismic response of SDG Slope. After converting the data into text files, the waveform data were baseline corrected and filtered through the Seismosignal software, then we obtained the three-component peak acceleration values of every group seismic wave at each monitoring station.

## 4. Drilling And Geophysical Investigation Methods

Two methods, electrical resistivity tomography and drilling, have been applied for geological conditions investigation at four monitoring sites. Detailed investigation routes and drilling positions are shown in Fig. 3a. Electrical resistivity tomography widely applied to various rock slope investigations is a kind of high-efficiency geophysical investigation method for collecting rich data (Jongmans and Garambois 2007). The method contains two parts, measuring and picture processing. By applying DC to underground media in shallow layers, arranging electrodes along the section to receive current from conductive media, and calculating apparent resistivity, we can know about the conductive performance of underground media and obtain the distribution situation of resistivity along the section. The apparent resistivity is the maximum in the distribution area of the gravel layer, relatively high in the shallow layers of bedrock, and the minimum in the distribution area of clay soil (Zhang 1979).

Three vertical sections have been determined according to the positions of monitoring sites in this paper and Wenner showing strong anti-interference capacity and stable observation results has been used for ERT measuring (Fig. 3a) (Schrott and Sass 2008; Naudet et al. 2008; Jongmans et al. 2009). The three vertical sections are respectively distributed upstream, midstream, and downstream of rock slope. The

GeoERT IP 2401 distributed high-density electrical prospecting apparatus and multi-functional digital DC system (240 channels, current measuring precision of  $\pm 0.1\%$ ) jointly developed by Lanzhou University and Beijing Geodesics Exploration Company, with the electrode spacing of 10 m and exploration depth reaching 140 m is applied in the study. All apparent resistivity sections are obtained after 5 times of iteration. The RMS deviation of the last iteration is controlled around 10 % to get the 2D apparent resistivity section along the measured section.

## 5. Data Processing And Methods

### 5.1 Seismic data analysis

All seismic events are recorded simultaneously by seismometers. Fig. 5 shows the three-component original records of the four seismometers. Before further analysis, we test the quality of the recorded seismic signals with the signal-to-noise ratio. After being pre-processed by baseline correction through Seismosignal software, the selected seismic data were filtered within the frequency scope of 0.5-20 Hz with Butterworth band-pass filter. The three-component peak acceleration of the seismic data recorded by seismometers can be directly obtained through the software. Taking the Monitoring Station P1 in the stable area as the reference, corresponding amplification times representing the relative difference of amplification coefficients at different sites can be obtained by comparing its peak acceleration with the three monitoring sites in the unstable area.

The horizontal-to-vertical spectral ratio (referred to here as HVSR) method is used to evaluate the amplification effect of local ground movement. This method was originally used to estimate the local field effect with ambient noise records (Nakamura 1989), then widely used to study the field response of different study areas under strong movement (Lermo and Chávez-García 1993; Panzera et al. 2017). Recently, the method had also been used to estimate the amplification effect of slope and landslide (Del Gaudio and Wasowski 2007). We have obtained corresponding resonance frequencies by studying the peaks of HVSR curves and took them as the indications for field resonance properties. Although the HVSR curve peak cannot present the actual amplification coefficient, it can be regarded as the indicator for the relative difference of amplification coefficient because of the complicated geological and geomorphological conditions of landslide areas (Del Gaudio et al. 2013). In this method, the data including hypocenter, propagation path, and media are consistent with the data of the same earthquake measured by the same seismometer. So the influence of these factors on studying the local seismic amplification effect of landslides can be eliminated by this method. The calculation method of HVSR is shown as Equation (1):

$$R_{ij}(f) = \frac{\sqrt{H_{1ij}(f)^2 + H_{2ij}(f)^2}}{V_{ij}(f)} = \frac{H_{ij}(f)}{V_{ij}(f)}, \quad (1)$$

Where  $H_{1ij}(f)$ ,  $H_{2ij}(f)$  and  $V_{ij}(f)$  respectively represent the Fourier spectrums of horizontal SN component, horizontal EW component, and vertical component of Field J in the earthquake event I.

The Geopsy software was applied to calculated HVSR curves. For every earthquake event, we converted three-component seismic waves into Fourier spectrums using the fast Fourier transform (FFT) method applied to 10 % cosine-tapered windows, then used the window function named Konno-Ohmanchi (Konno and Ohmachi 1998) to smoothen spectrums and calculated HVSR curves through Equation (1) at last.

## 5.2 Drilling and Electrical Resistivity Tomography

Drill rock stone with the  $\varphi$  75 mm diamond drill bit and double-layer rock core pipe for continuous coring. Among the rock core obtained by drilling, the ratio between the accumulative length of all rock core sections longer than 10 cm and the drilling footage can reflect the integrity of rock and development of crack in the strata of this section.

The apparent resistivity 2D section obtained by image processing of electrical resistivity tomography is processed through the least-mean-square algorithm (Loke 1999) and RES2DINV software and obtained by defective data points elimination, topographical correction, RMS convergence-constraint method, and the least-squares inversion successively. During the least-squares inversion process, it is applicable to adapt to different types of geological structures by adjusting the damping coefficient and smoothness-to-filtering ratio (Naudet et al. 2008).

## 6. Results

### 6.1 Peak Acceleration Ratio Curve Characteristics

Take the Monitoring Station P1 located at the highest altitude in the stable area as the reference, the amplification times calculated based on the ratios of Monitoring Stations P2, P3, and P4 in the unstable area to the reference are presented in Fig. 6. With the elevation change, the three-component peak acceleration amplification times of seismic waves show the same trend, which results in a “convex” type response. All the three-component amplification times of the three monitoring stations in the unstable slope area are greater than 1. The three-component amplification times at Monitoring Station P2 are 1.56, 1.74, and 1.71, at Monitoring Station P3, are 1.49, 1.67, and 1.47, at Monitoring Station P4, are 1.39, 1.66, and 1.49. Among them, amplification times of Monitoring Station P2 are the largest.

The aspect of SDG slope is  $78^\circ$ . The intersection angles between SDG Slope aspect and the connecting line of hypocenter and SDG Slope are divided into five classes, which are  $0-30^\circ$ ,  $30-90^\circ$  (for too little data of  $30-60^\circ$  and  $60-90^\circ$ , these two groups are integrated as a whole for statistical analysis to prevent the influence of random error),  $90-120^\circ$ ,  $120-150^\circ$  and  $150-180^\circ$ . The PGA amplification times of three-component seismic waves at monitoring stations are shown in Fig. 7. It can be seen from Fig. 7 that the peak acceleration grows when the intersection increases. In other words, the peak accelerations of monitoring stations are the smallest when the intersection angle is  $0-30^\circ$ , namely, the seismic waves travel in the opposite direction of the slope. When seismic waves travel in the same direction of the slope, namely the intersection angle is  $160-180^\circ$ , the peak accelerations of monitoring stations are the largest.

According to the comparison results of the mean amplification times of three monitoring stations in the same intersection scope, as shown in Fig. 8, the amplification times of Monitoring Station P2 is the largest, followed by Monitoring Station P3, and the amplification times of Monitoring Station P4 is the smallest.

## 6.2 HSVR Curve Characteristics

The HVSr curves obtained by calculating the seismic data monitored at monitoring sites can be found in Fig. 9. At Station P1, HVSr curves are amplified significantly in the frequency scope of 12.1–14.8 Hz, with a mean peak value of 2.6. At Monitoring Station P2, curves are significantly amplified in the frequency scope of 5.6–6.2 Hz with a mean peak of 3.51. At Monitoring Station P3, the curves are significantly amplified in the frequency scope of 2.8–3.9 Hz with a mean peak of 3.01. And at Monitoring Station P4, the curves are significantly amplified in the frequency scope of 2.5–3.2 Hz with the mean peak of 2.64. By putting peak amplification coefficient mean values across the entire frequency range of all monitoring sites in Fig. 10, it is found that the amplification effect of monitoring stations on the unstable slope in the lower part is more intense than the monitoring station on the stable slope in the upper part, which is same as the peak acceleration ratio conclusion. Regarding the three monitoring stations on the unstable slope, the amplification coefficient of Monitoring Station P2 is greater than Monitoring Stations P3 and P4.

## 6.3 Rock Core and Resistivity

Six kinds of lithology can be obtained by drilling (as shown in Fig. 11). The deposits loose of shallow overburden at the depth of 5–14 m are composed of yellow silty soil with gravel which is slightly wet and plastic. Moderately weathered phyllite can be observed at the depth of 7–20 m, with the rock structure damaged in some parts and relatively developed cracks. The intensely weathered fragmented rock mass can be observed at the depth of 5–60m, showing fragmented structure. The gray-black silty clay observed at the depth of 40–70 m is extremely weathered phyllite, slightly wet, plastic, mixed with a small amount of broken stone. And the gray-black carbon phyllite in Upper Formation of the Devonian Weiguan Group is visible at the depth of 20–80 m. No groundwater is detected throughout the drilling process.

In addition, we have recorded the RQD values of rock core drilled at three places (Fig. 12). The RQD value of the rock core throughout the drilling depth of borehole Z01 (P4) is close to 0 %. For borehole Z02 (P2), the RQD value is close to 0 % above 23 m, around 10 % at the depth of 8 m and 12 m, greater than 50 % below 23 m, and 80 % at the maximum. For borehole Z03 (P3), the RQD value is close to 0 % at the depth of 0–62 m, then surges to 50 % at maximum while getting deeper.

The underground resistivity distribution of the whole section line is investigated by electrical resistivity tomography method. Figure 13 only presents the underground lithofacies' apparent resistivity distribution around four monitoring sites, as only the local seismic response at monitoring sites is studied in this paper. On the stable part of SDG Slope, only relatively complete bedrock mass with the resistivity greater

than 400 Ohm.m is distributed under P1. On the unstable part of SDG slope, the rock mass above 10 m at P2 shows the resistivity alternately presented in high and low values. At the same site, the resistivity ranges from 50 to 100 Ohm.m at the depth of 10–25 m and is greater than 300 Ohm.m below 25 m. The resistivity of P3 seems alternately high and low above 5 m, changes in the range of 10–50 Ohm.m at the depth of 5–55 m and is greater than 300 Ohm.m below 55 m. For P4, the resistivity is alternately high and low above 15 m, in the range of 10–50 Ohm.m at the depth of 15–70 m and above 300 Ohm.m below 70 m.

We have divided the underground structure of the three monitoring sites (P2, P3, and P4) in the unstable area into six types according to the lithological characteristics of boreholes, rock core RQD values, and apparent resistivity values, which are the loose deposit of shallow overburden, moderately weathered rock mass, fragmented rock mass, highly weathered phyllite, rock mass at the inferred slip surface and phyllite (Fig. 14). According to the borehole histogram in Fig. 13, the Monitoring Station P2 (Z02) is composed of lithofacies 1 above 7.2 m, lithofacies 2 at the depth of 7.2–19.1 m, lithofacies 5 at the depth of 19.1–22.8 m, and lithofacies 6 below 22.8 m. The Monitoring Station P3 (Z03) is composed of lithofacies 1 above 5.4 m, lithofacies 3 at the depth of 5.4–56.5 m, lithofacies 5 at the depth of 56.5–61 m, and lithofacies 6 below 61 m. And the Monitoring Station P4 (Z01) is made of lithofacies 1 above 13.5 m, lithofacies 3 at the depth of 1.5–42.3 m, lithofacies 4 at the depth of 57.1–70.5 m, and lithofacies 4 at the depth of 70.5–75 m, without bedrock (lithofacies 6).

## 7. Discussion

We found based on the field monitoring data that compared with the higher elevation P1 located on the stable part of SDG slope, P2, P3, and P4 located on the unstable area of SDG slope at a lower altitude have larger ground motion response amplification coefficient. Even the Stations P2 and P3 similar in elevation have different ground motion response amplification coefficients. If ranking the four stations by seismic response amplification coefficients, P2 is the largest, followed by P3, P4, and P1 in succession. The same rule is also found in the site-epicenter azimuth. With the increasing intersection between SDG Slope aspect and the connecting line of hypocenters and SDG Slope, the seismic amplification coefficient of the monitoring station grows (Fig. 7). The growth is caused by the full reflection of vertically incident seismic waves on the surface of the slope when the epicenter is on the back of the slope, which leads to the superimposition of seismic wave and acceleration multiplication and makes the seismic amplification effect more obvious (Cho and Kaneko 2004; Tang et al. 2009; Li et al. 2013). Besides, the seismic response is amplified abnormally on the top of ridges, and slopes, and tower-like rock mass (Celebi 1987; Huang and Chiu 1999; Shen et al. 2019). When the incident wavelength is equivalent to terrain width, the seismic amplification response in higher places is more intensive, while lower places have no amplification response or less intensive amplification response according to Boore (1972) and Bouchon (1973). The same phenomenon is also revealed by Luo et al. (2020) and He et al. (2020) through numerical simulation (e.g., Celebi 1985; Luo et al. 2020; Shen et al. 2019). To judge if our terrain meets the conditions of elevation amplification, we applied the empirical formula for theoretical resonance frequency for topographic effect calculation (Geli et al. 1988).

$$f_t = \frac{V_s}{L}, \quad (2)$$

in which  $V_s$  is shear wave velocity,  $L$  is the base width of a slope, and  $f_t$  is the topographic resonance frequency.

To prevent calculation from being affected by the shallow surface lithofacies, shear wave velocity shall be the shear wave velocity of bedrock. According to Wang et al (2018) and Luo et al. (2021), we set the bedrock shear wave velocity of phyllite formation at 2000 m/s. For the hill slope where SDG Slope is located, we set the base width of the slope at 2000 m. By Equation (2), we obtained that  $f_t$  is 1 Hz. While corresponding frequencies of the maximum amplitudes of Monitoring Stations P2, P3, and P4 are 5.6-6.2 Hz, 2.8-3.9 Hz, and 2.5-3.2 Hz respectively, which are quite different from the calculation result. So we speculate that the amplification effect intensity of unstable mass is decided by the geological conditions.

As researchers reported that overburden and loose soil filtered high-frequency seismic waves and amplified low-frequency ones (Wang 2012; Luo et al. 2021). It was found by Danneels (2008) through field monitoring that the thick loess overburden had a more intensive amplification response than the thinner one. And Ma et al. (2019) also found that the amplification effect of the site above slope deposit was far greater than bedrock by monitoring the amplification effects of two places in the same elevation at slope toe. Burjánek et al. (2012) argued that the elastic modulus of unstable rock mass was lower than complete bedrock. Seismic impedance occurred at the boundary of broken rock mass and perfect bedrock, which may capture incident waves. Unstable rock mass played the role of a resonator, making standing waves develop in the broken rock mass. While the surface of the slope as a free face showed the largest amplitude. The minimum mean value of the amplification coefficients at the three monitoring sites in the unstable slope area is 2.64. According to the HVSR standard of SASAME (2004), it can be regarded as the amplification effect that exists when the amplification coefficient is greater than 2. And when the amplification coefficient is 4, the rock slope is very weak according to Kleinbrod et al. (2017). As amplification coefficient mean value obtained by us in this paper up to 3.5, it can be concluded that SDG Slope is very weakened.

Seismic impedance can be found on the boundary of weak rock mass and bedrock. Danneels (2008) found that the loess overburden with the minimum apparent resistivity of only 5 Ohm.m and the underlying bedrock with the minimum apparent resistivity of 300 Ohm.m had led to 6 times the seismic amplification. Ma et al. (2019) found that the seismic amplification up to 20 had been caused by the impedance contrast between the rock layer with the resistivity of 3500 Ohm.m and the one with the resistivity of 2500 Ohm.m. As HVSR curve amplitude is directly proportional to impedance contrast of seismic wave (Oubaiche et al. 2012; Uebayashi et al.; 2012; Hartzell et al. 2017), the HVSR curve amplitude can reflect the magnitude of the impedance contrast. However, the seismic response amplification coefficient in the unstable part of the slope monitored by us is only 2.64-3.51, smaller than the amplification coefficient monitored by Danneels (2008) and Ma et al. (2019). The minimum bedrock resistivity in our study area is about 300 Ohm.m, while the apparent resistivity of rock mass (lithofacies

2) below Monitoring Station P2 with the highest amplification coefficient is 50-300 Ohm.m, with the resistivity difference far smaller than the values reported by Danneels (2008) and Ma et al. (2019). Although the relationship between resistivity difference and seismic amplification is still unclear yet, the resistivity difference may be the cause of the small seismic amplification coefficient. In addition, both epicentral distance and earthquake magnitude are smaller than the reports of Danneels (2008) and Ma et al. (2019) may also be the reasons for the small seismic response amplification. We speculate that the fragmentation degree of rock mass gets worse along with the deformation of the unstable slope, which results in the increase of apparent resistivity between unstable body and bedrock and rising of seismic amplification coefficient.

We also found that the seismic response is inversely proportional to the thickness of the unstable slope. In other words, the seismic response of Monitoring Station P2 in the thin part of the unstable slope is more intensive than that of Monitoring Stations P3 and P4 in the thick part of the unstable slope, which is totally contrary to the conclusion of Danneels (2008) who took overburden as the object to study and found that the amplification intensity was directly proportional to the thickness. Different from Monitoring Station P2, a layer of fragmented rock mass containing mud (Lithofacies 3) with the resistivity of 10-50 Ohm.m and gray-black silty clay (Lithofacies 4) exist between bedrock and Lithofacies 2 in both Stations P3 and P4. According to Danneels (2008), the apparent resistivity of the surface layer of loess is also less than 50 Ohm.m, and the apparent resistivity of the underlying bedrock is greater than 300-1200 Ohm.m, but the apparent resistivity of the central part is 50-300 Ohm.m, so overall the apparent resistivity increases with increasing depth. While a weak layer with the apparent resistivity of 10-50 Ohm.m is developed in the substructure of Monitoring Stations P3 and P4, which may restrain the seismic response (Xu et al. 2003; Hartzell et al. 2017). So weak layer may play a seismic isolation effect between two lithofacies with greater elastic modulus.

## 8. Conclusion

By calculating the peak acceleration ratio with station P1 as the reference point, it is found that the three monitoring stations at lower altitudes in the unstable area show an obvious amplification effect. The seismic impedance ratio at the boundary of fragmented rock mass and bedrock makes the unstable slope exhibit the seismic amplification effect, by which we can identify the slope scope. If the intersection between seismic wave propagation direction and slope direction reduces, the seismic response amplification coefficients of the three monitoring stations in the slope area increase. Namely, the seismic response is the maximum when the epicenter is on the back of a slope. If there is low-resistivity fine-grained soil in the unstable rock mass, the fine-grained will absorb the shock under certain conditions, weakening the seismic response on the surface of a slope.

## Declarations

## Acknowledgments

This study was supported by the National Key R&D Program of China (Grants No. 2017YFC1501002), the National Natural Science Foundation of China (Grants No. 41931296, 41907254, 41521002).

**Funding** This study was supported by the National Key R&D Program of China (Grants No. 2017YFC1501002), the National Natural Science Foundation of China (Grants No. 41931296, 41907254, 41521002).

**Conflict of interest** The authors declare that they have no known competing financial interests or personal relationships that could have appeared to influence the work reported in this paper.

**Availability of data and material** Information on the occurrence time, magnitude, focal depth, and other information of the seismic event monitored by seismometers in this article can be found in China Earthquake Network Center (<https://news.ceic.ac.cn/index.html?time=1630826315>). The other processed data required to reproduce these findings cannot be shared at this time as the data also forms part of an ongoing study.

**Code availability** Not applicable.

**Ethical approval** Not applicable.

**Consent to participate** Not applicable.

**Consent for publication** Not applicable.

## References

Acerra C, Havenith HB, Zacharopoulos, S (2004) Guidelines for the implementation of the H/V spectral ratio technique on ambient vibrations measurements, processing and interpretation (No. European Commission–EVG1-CT-2000-00026 SESAME). European Commission

Boore, DM (1972) A note on the effect of simple topography on seismic SH waves. *Bulletin of the seismological Society of America* 62:275-284

Bouchon M (1973) Effect of topography on surface motion. *Bulletin of the Seismological Society of America* 63:615-632

Burjáne J, Moore JR, Yugsi Molina, FX, and Fäh D (2012) Instrumental evidence of normal mode rock slope vibration. *Geophysical Journal International* 188:559-569

Celebi M (1987) Topographical and geological amplifications determined from strong-motion and aftershock records of the 3 March 1985 Chile earthquake. *Bulletin of the Seismological Society of America* 77:1147-1167

- Cho SH, Kaneko K (2004) Influence of the applied pressure waveform on the dynamic fracture processes in rock. *International Journal of Rock Mechanics and Mining Sciences* 41:771-784.
- Danneels G, Bourdeau C, Torgoev I, Havenith HB (2008) Geophysical investigation and dynamic modelling of unstable slopes: case-study of Kainama (Kyrgyzstan). *Geophysical Journal International* 175:17-34.
- Del Gaudio V, Wasowski J (2007) Directivity of slope dynamic response to seismic shaking. *Geophysical research letters* 34
- Gaudio VD, Wasowski J, Muscillo S (2013) New developments in ambient noise analysis to characterise the seismic response of landslide-prone slopes. *Natural hazards and earth system sciences* 13:2075-2087
- Geli L, Bard PY, Jullien B (1988) The effect of topography on earthquake ground motion: a review and new results. *Bulletin of the Seismological Society of America* 78:42-63
- Gischig V, Preisig G, Eberhardt E (2016) Numerical investigation of seismically induced rock mass fatigue as a mechanism contributing to the progressive failure of deep-seated landslides. *Rock Mechanics and Rock Engineering* 49:2457-2478
- Huang HC, Chiu HC (1999) Canyon topography effects on ground motion at Feitsui dam site. *Soil Dynamics and Earthquake Engineering* 18:87-99
- He J, Qi S, Wang Y, Saroglou C (2020) Seismic response of the Lengzhuguan slope caused by topographic and geological effects. *Engineering Geology* 265:105431
- Hartzell S, Meremonte M, Ramírez-Guzmán L, and McNamara D (2014) Ground motion in the presence of complex topography: Earthquake and ambient noise sources. *Bulletin of the Seismological Society of America* 104:451-466
- Hartzell S, Leeds AL, Jibson RW (2017) Seismic response of soft deposits due to landslide: The Mission Peak, California, landslide. *Bulletin of the Seismological Society of America* 107:2008-2020
- Jongmans D, Garambois S (2007) Geophysical investigation of landslides: a review. *Bulletin de la Société géologique de France* 178:101-112
- Jongmans D, Bièvre G, Renalier F, Schwartz S, Beaurez N, and Orengo Y (2009) Geophysical investigation of a large landslide in glaciolacustrine clays in the Trièves area (French Alps). *Engineering Geology* 109:45-56
- Konno K., Ohmachi T (1998) Ground-motion characteristics estimated from spectral ratio between horizontal and vertical components of microtremor. *Bulletin of the Seismological Society of America* 88:228-241

- Kleinbrod U, Burjánek J, and Fäh D (2017) On the seismic response of instable rock slopes based on ambient vibration recordings. *Earth, Planets and Space* 69:1-9
- Leonov NN (1960) The Khait, 1949 earthquake and geological conditions of its origin. *Proceedings of Academy of Sciences of the USSR, Geophys, Series, 3* 409-424
- Lermo J, and Chávez-García FJ (1993) Site effect evaluation using spectral ratios with only one station. *Bulletin of the seismological society of America* 83:1574-1594
- Loke MH (1999) *Electrical imaging surveys for environmental and engineering studies. A practical guide to 2 70*
- Lee SJ, Komatitsch D, Huang BS, Tromp J (2009) Effects of topography on seismic-wave propagation: An example from northern Taiwan. *Bulletin of the Seismological Society of America* 99:314-325
- Li W, Xu Q, Huang R (2013) Preliminary study on back slope effect of landslide in Wenchuan Earthquake. *Acta Geology* 87:294-295 (**in Chinese**)
- Li LQ, Ju NP, Zhang S, Deng XX, Sheng D (2019) Seismic wave propagation characteristic and its effects on the failure of steep jointed anti-dip rock slope. *Landslides* 16:105-123
- Luo Y, Fan X, Huang R, Wang Y, Yunus AP, Havenith HB (2020) Topographic and near-surface stratigraphic amplification of the seismic response of a mountain slope revealed by field monitoring and numerical simulations. *Engineering Geology* 271:105607
- Luo Y, Lei W, Wang Y, Zhu X, Ou J (2021) Revealing the geological materials properties by a shallow seismic method for investigating slope site effects: a case study of Qiaozhuang town, Qingchuan County, China. *Arabian Journal of Geosciences* 14:1-15
- Ma N, Wang G, Kamai T, Doi I, Chigira M (2019) Amplification of seismic response of a large deep-seated landslide in Tokushima, Japan. *Engineering Geology* 249:218-234
- Naudet V, Lazzari M, Perrone A, Loperte A, Piscitelli S, Lapenna V (2008) Integrated geophysical and geomorphological approach to investigate the snowmelt-triggered landslide of Bosco Piccolo village (Basilicata, southern Italy). *Engineering Geology* 98:156-167
- Nakamura Y (1989) A method for dynamic characteristics estimation of subsurface using microtremor on the ground surface, Railway Technical Research Institute, Quarterly Reports. 30
- Oubaiche EH, Chatelain JL, Bouguern A, Bensalem R, Machane D, Hellel M, Guillier B (2012) Experimental relationship between ambient vibration H/V peak amplitude and shear-wave velocity contrast. *Seismological Research Letters* 83:1038-1046

Panzer F, Halldorsson B, Vogfjörð K (2017) Directional effects of tectonic fractures on ground motion site amplification from earthquake and ambient noise data: a case study in South Iceland. *Soil Dynamics and Earthquake Engineering* 97:143-154

Schrott L, Sass O (2008) Application of field geophysics in geomorphology: advances and limitations exemplified by case studies. *Geomorphology* 93:55-73

Shen T, Wang YS, Luo YH, Xin CC, Liu Y, He JX (2019) Seismic response of cracking features in Jubao Mountain during the aftershocks of Jiuzhaigou Ms7. 0 earthquake. *Journal of Mountain Science* 16:2532-2547

Song D, Chen Z, Ke Y, Nie W (2020) Seismic response analysis of a bedding rock slope based on the time-frequency joint analysis method: a case study from the middle reach of the Jinsha River, China. *Engineering Geology* 274:105731

Tang C, Zuo Y, Qin S, Yang J, Wang D, Li L, Xu T (2009) Spalling and slinging i pattern of shallow slope and dynamics explanation in the 2008 Wenchuan earthquake. *Proceedings of the 10th Conference on Rock Mechanics and Engineering, China*. 258-262 **(in Chinese)**

Uebayashi H, Kawabe H, Kamae K (2012) Reproduction of microseism H/V spectral features using a three-dimensional complex topographical model of the sediment-bedrock interface in the Osaka sedimentary basin. *Geophysical Journal International* 189:1060-1074

Wang Y, Luo Y, Wang F, Wang D, Ma X, Li S, Deng X (2012) Slope seismic response monitoring on the aftershocks of the Wenchuan earthquake in the Mianzhu section. *Journal of Mountain Science* 9:523-528

Wang Y, Zhao B, Li J (2018) Mechanism of the catastrophic June 2017 landslide at Xinmo Village, Songping River, Sichuan Province, China. *Landslides* 15:333-345

Xu H, Chen D, Yang X, Liang B (2003) Propagation Characteristics of plane SH wave passing through elastic interlining in elastic medium propagation. *Journal of Rock Mechanics and Geotechnical Engineering* 22:304-308 **(in Chinese)**

Zhang X (1979) *Engineering Geology, Volume 2*. Seismological Press, Beijing, pp 28-31 **(in Chinese)**

## Figures

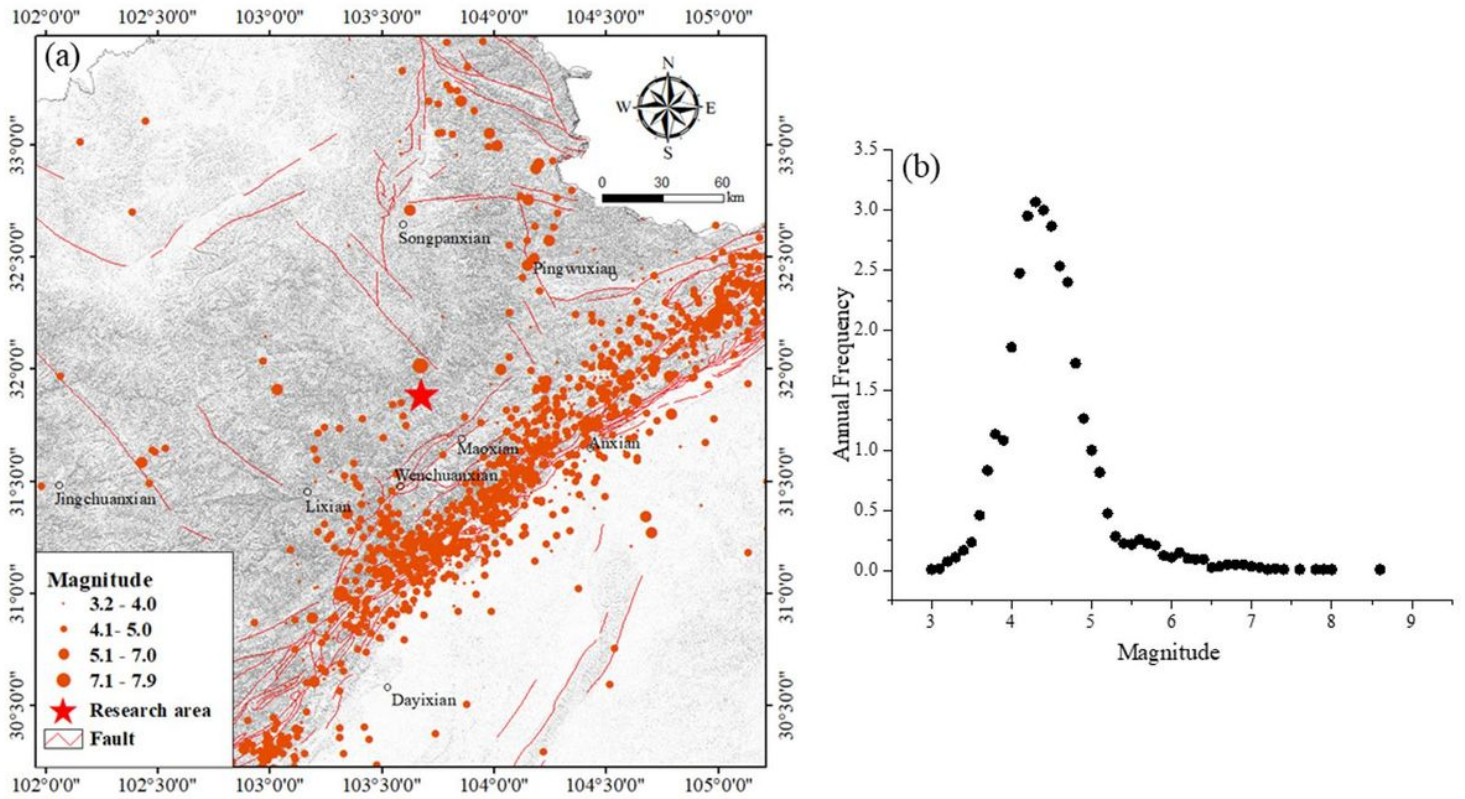


**Figure 1**

a Location of Study Area and Situation of Historical Earthquakes Happened Since 1990, b Annual Occurrence Frequency of Historical Earthquakes in Different Magnitudes Happened Since 1990 around Study Area

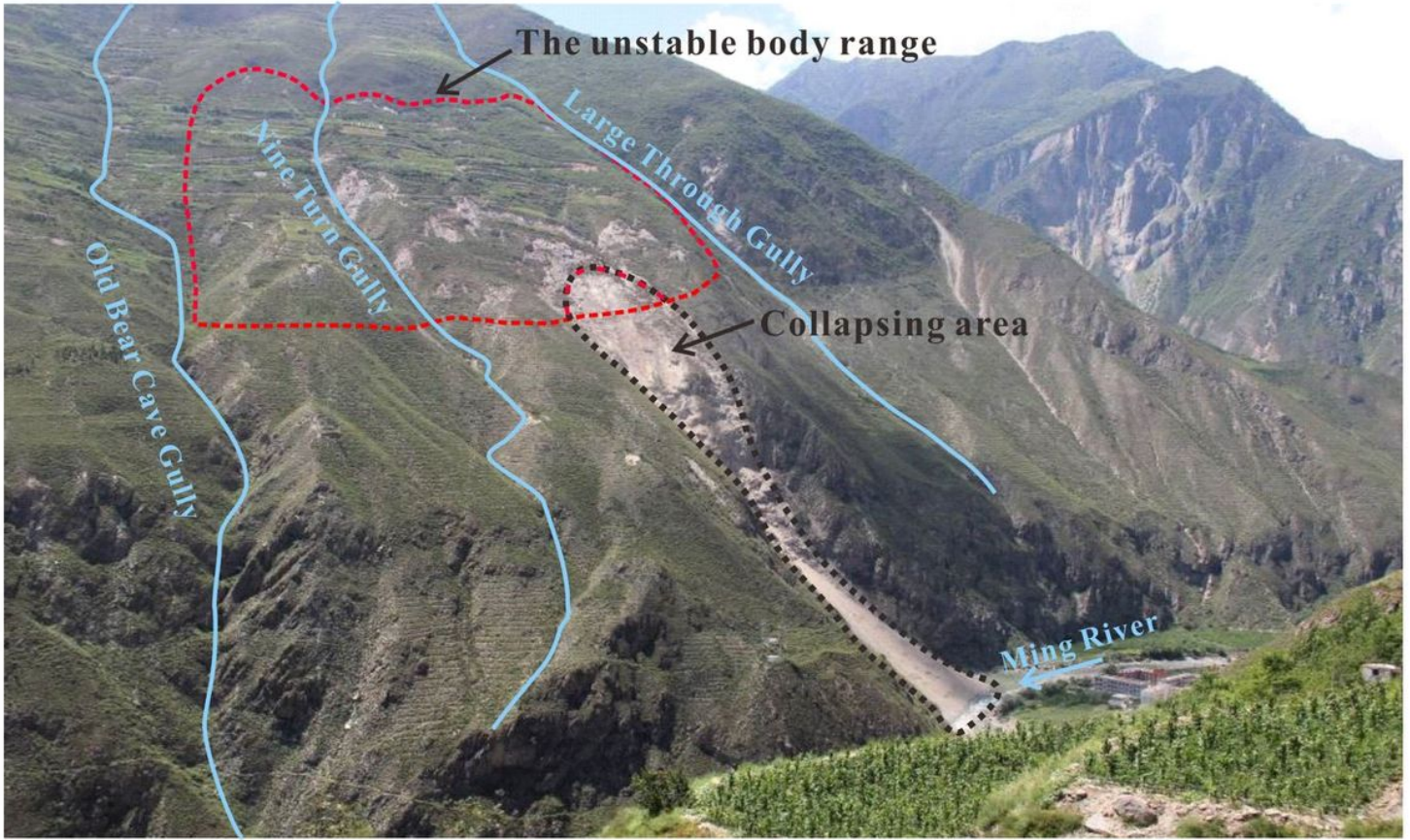
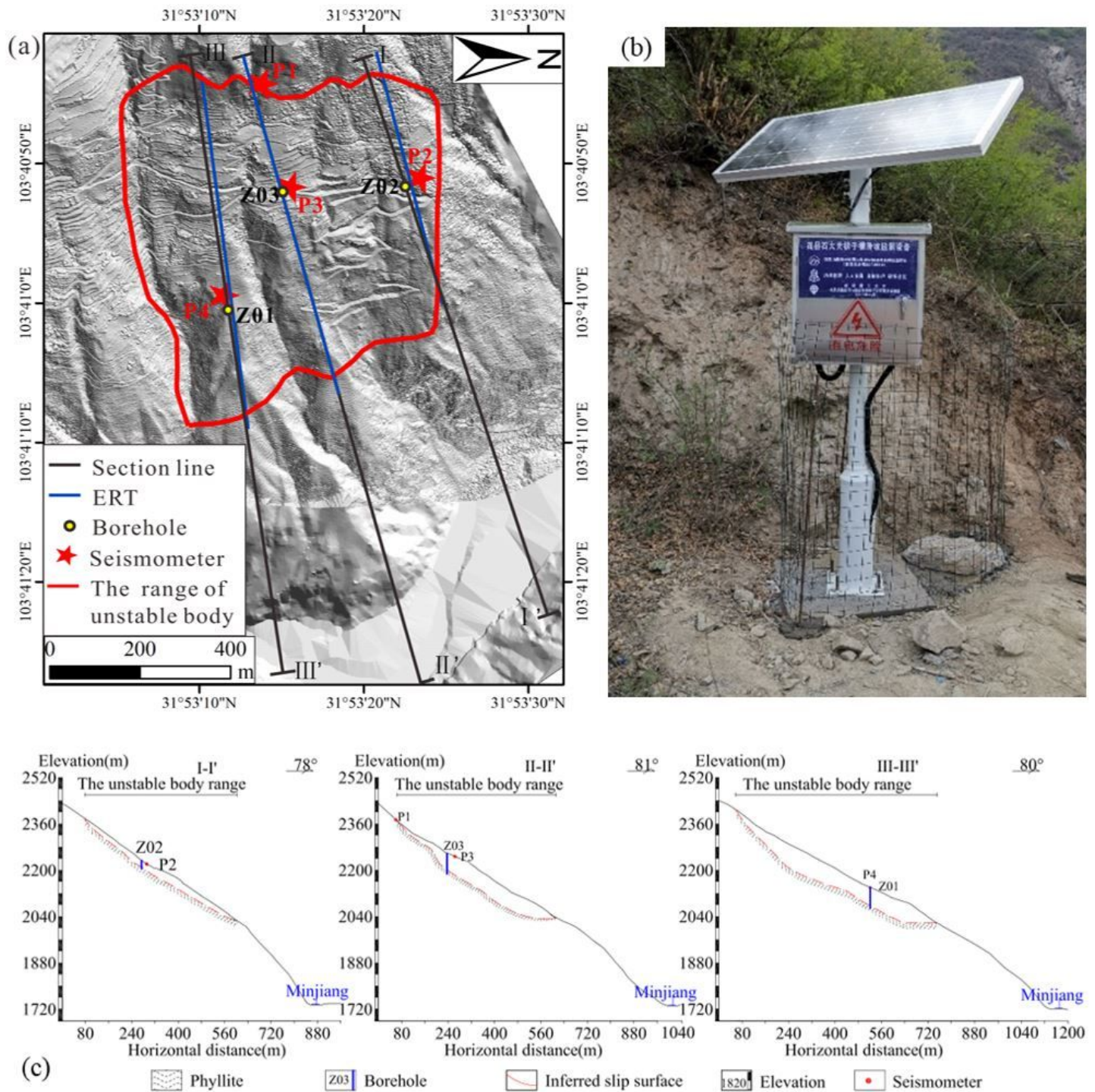


Figure 2

Full View of SDG Slope



**Figure 3**

a Plan Layout of Monitoring Sites in Geophysical Survey Diagram (Red stars are seismic monitoring sites, blue lines are sections obtained by electro-physical survey, yellow circles are boreholes), b Field Installation Diagram of Seismometer, c Section Map (Showing the locations of the four seismometers)

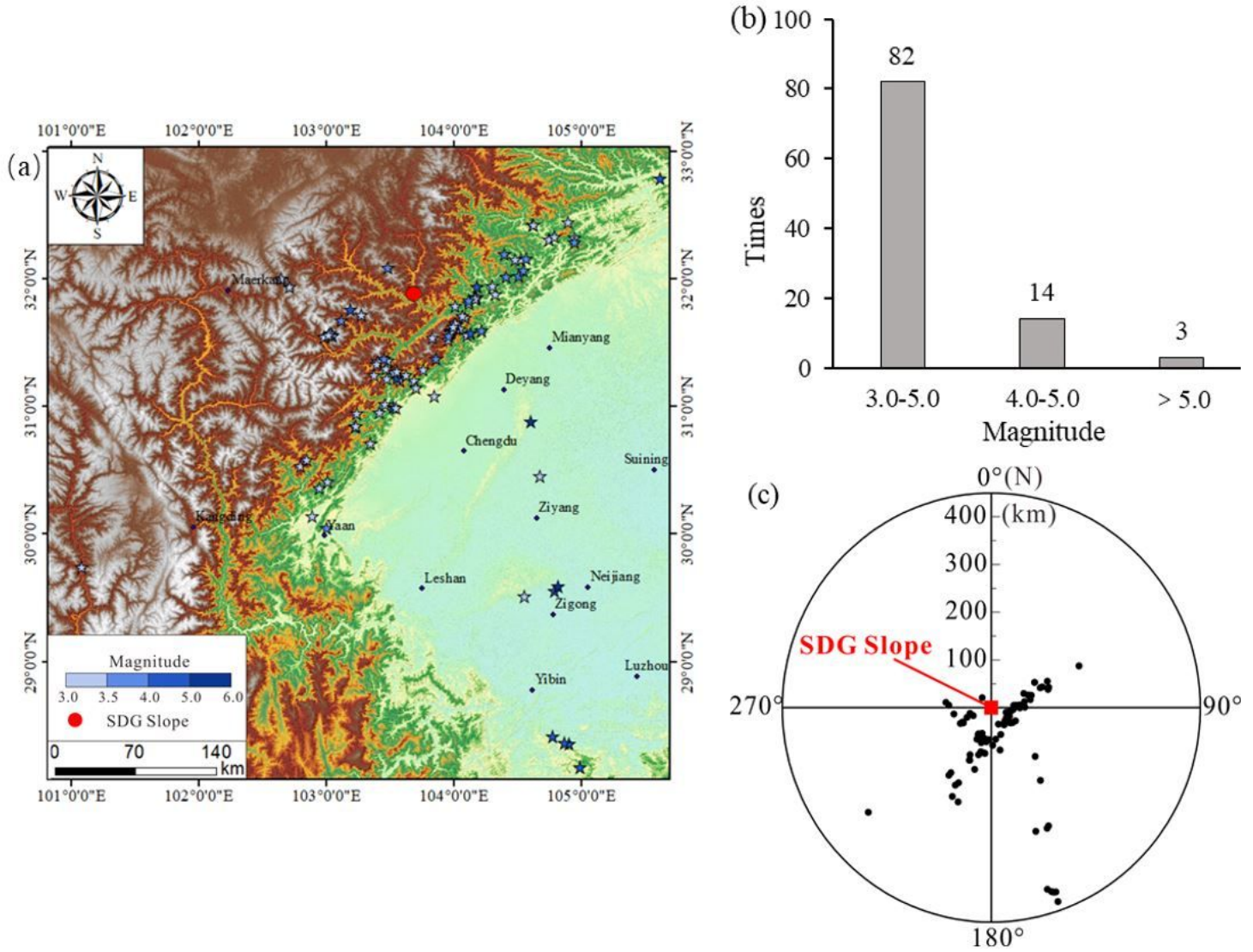


**Figure 4**

a Epicentral Distribution Recorded from July 2019 to April 2021 (earthquakes of different magnitudes are represented by different colors of starts), b Magnitude Distribution in Monitored Earthquake Statistics, c Distance between Epicenter and Rock Slope and the site-epicenter azimuth (Epicentral distance is drawn long the radius of the diagram)

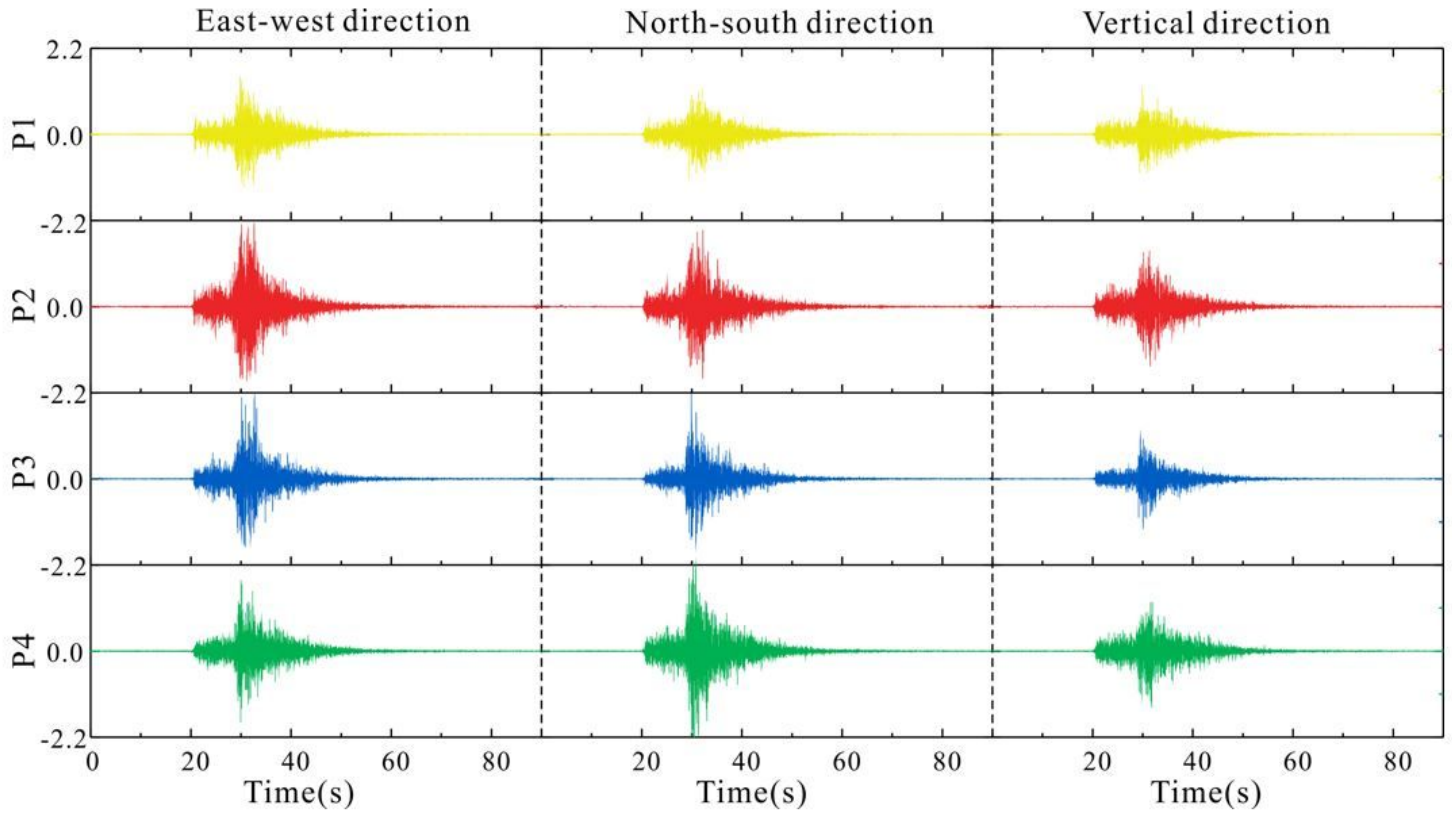


**Figure 5**

Three-component Acceleration Time Curves Recorded by Four Seismometers on April 26, 2020

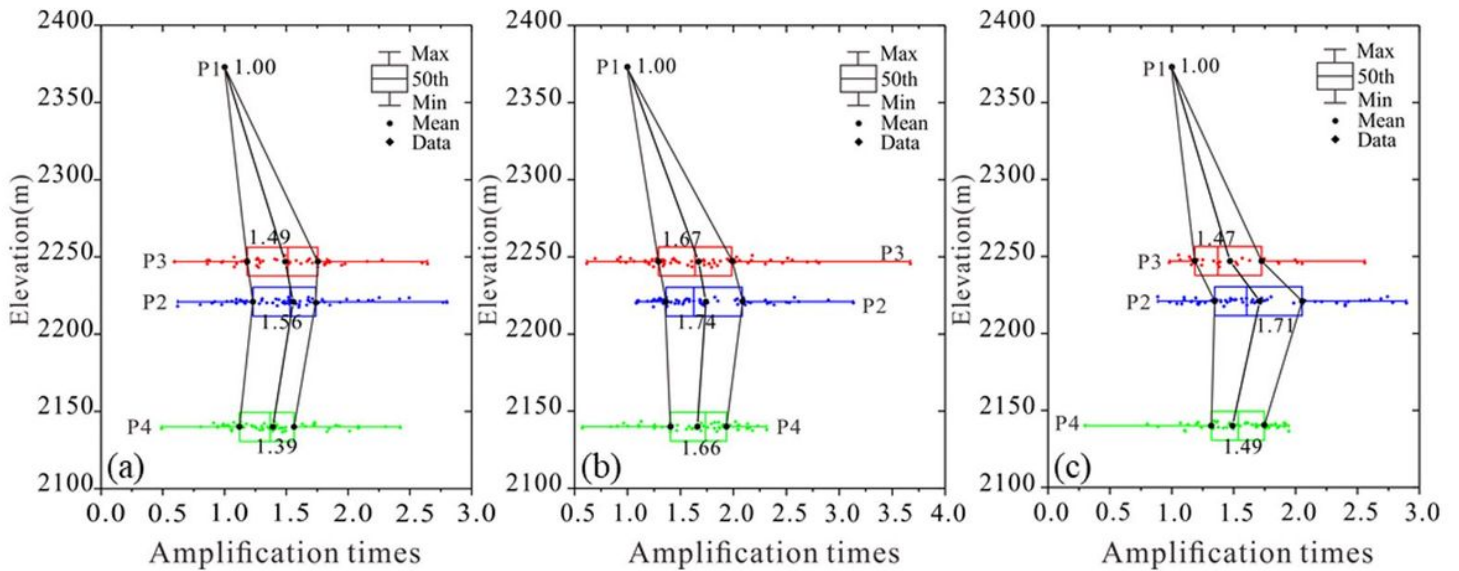


**Figure 6**

Amplification Times of Station P1: a Horizontal EW Direction, b Horizontal SN Direction, c Vertical Direction

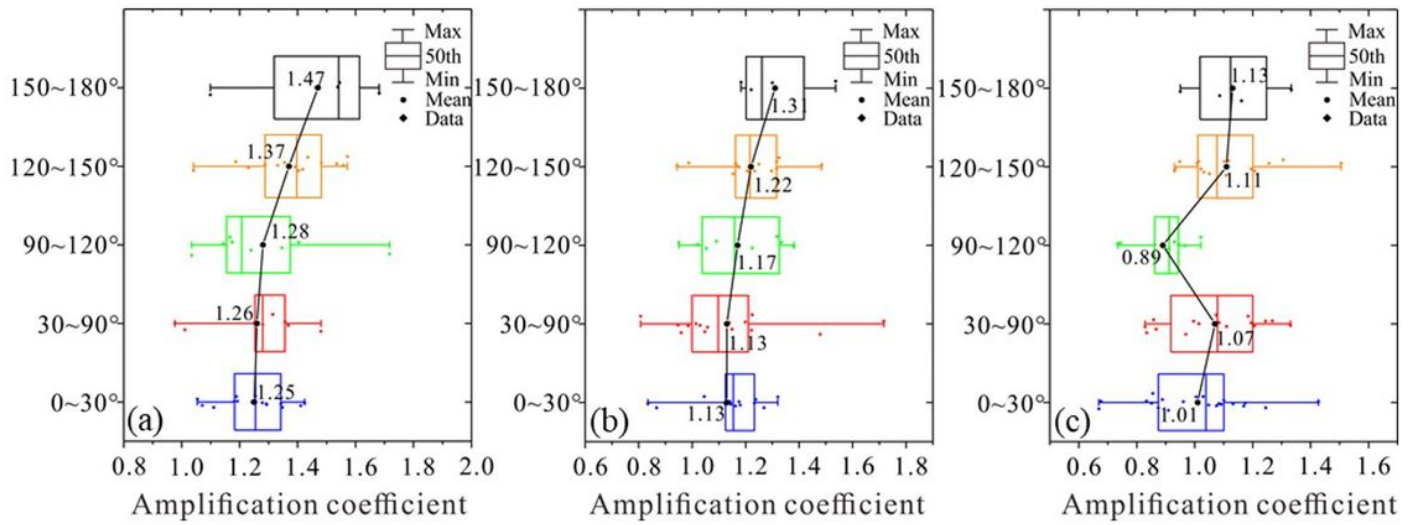


Figure 7

Changes of Amplification Coefficient with Site-epicenter Azimuth: a P2, b P3, c P4

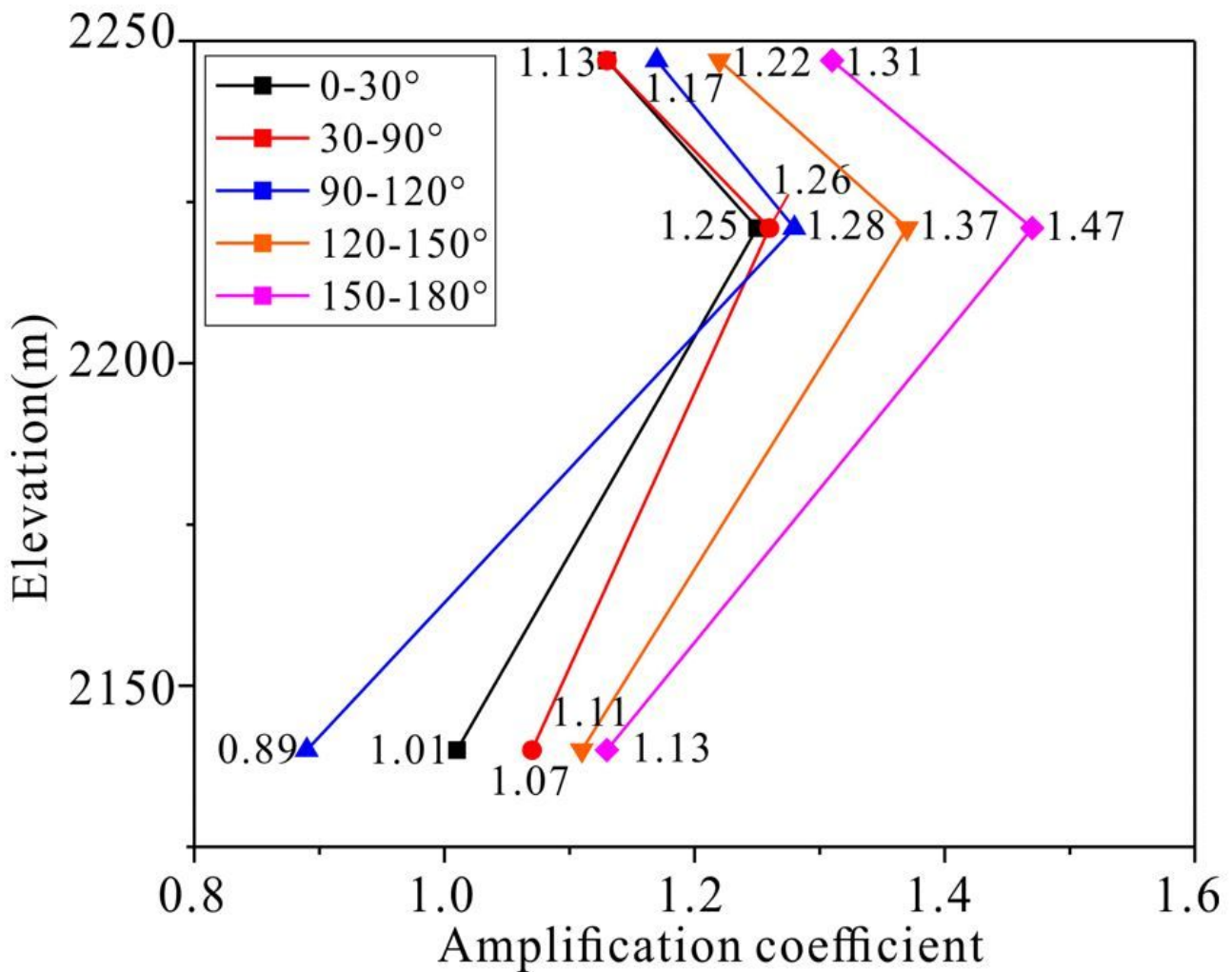


Figure 8

Changes in Amplification Coefficients of P2, P3, and P4 in Different Intersections

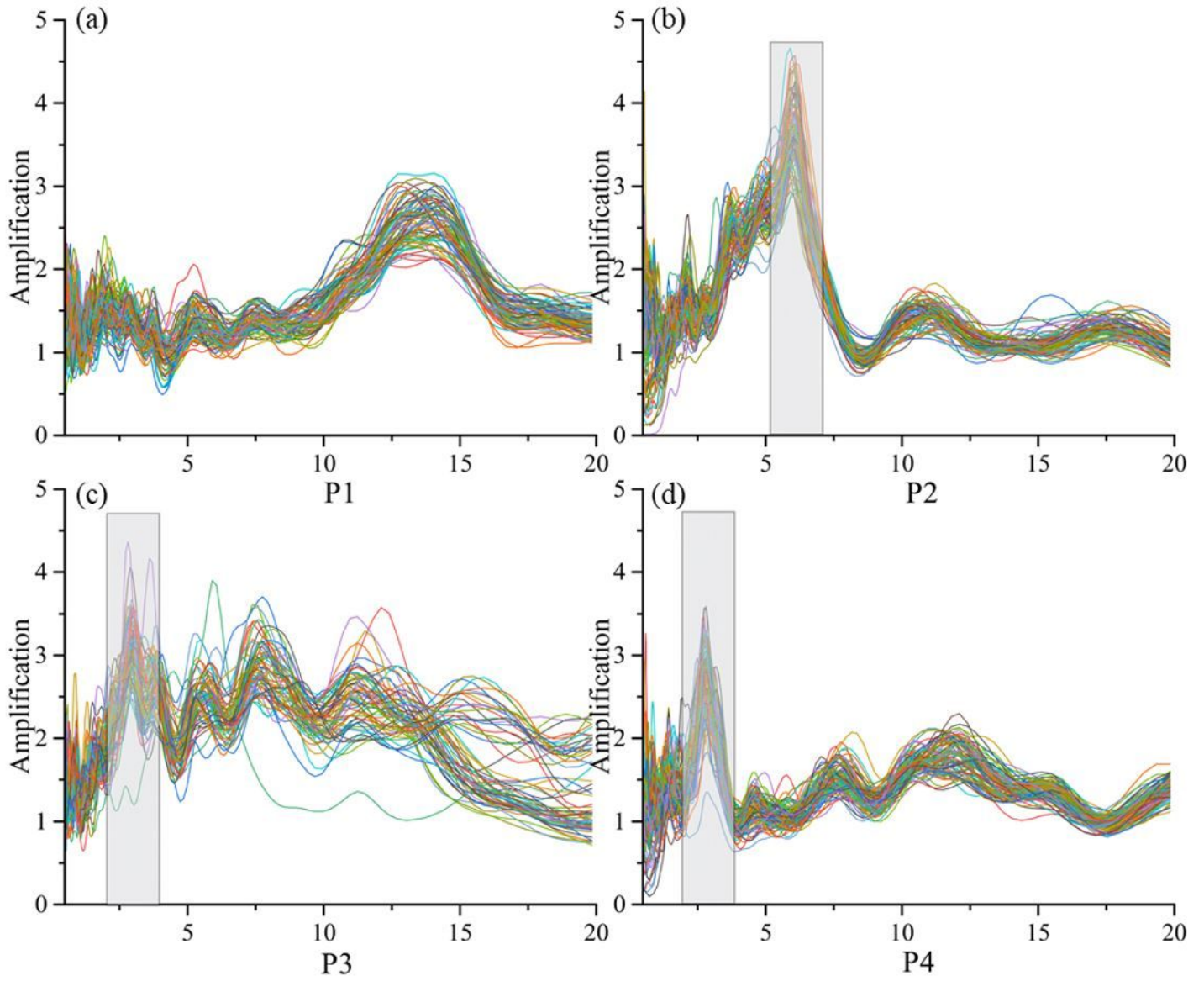


Figure 9

HVSR Curves Chart of Monitored Seismic Data: a Station P1, b Station P2, c Station P3, d Station P4.

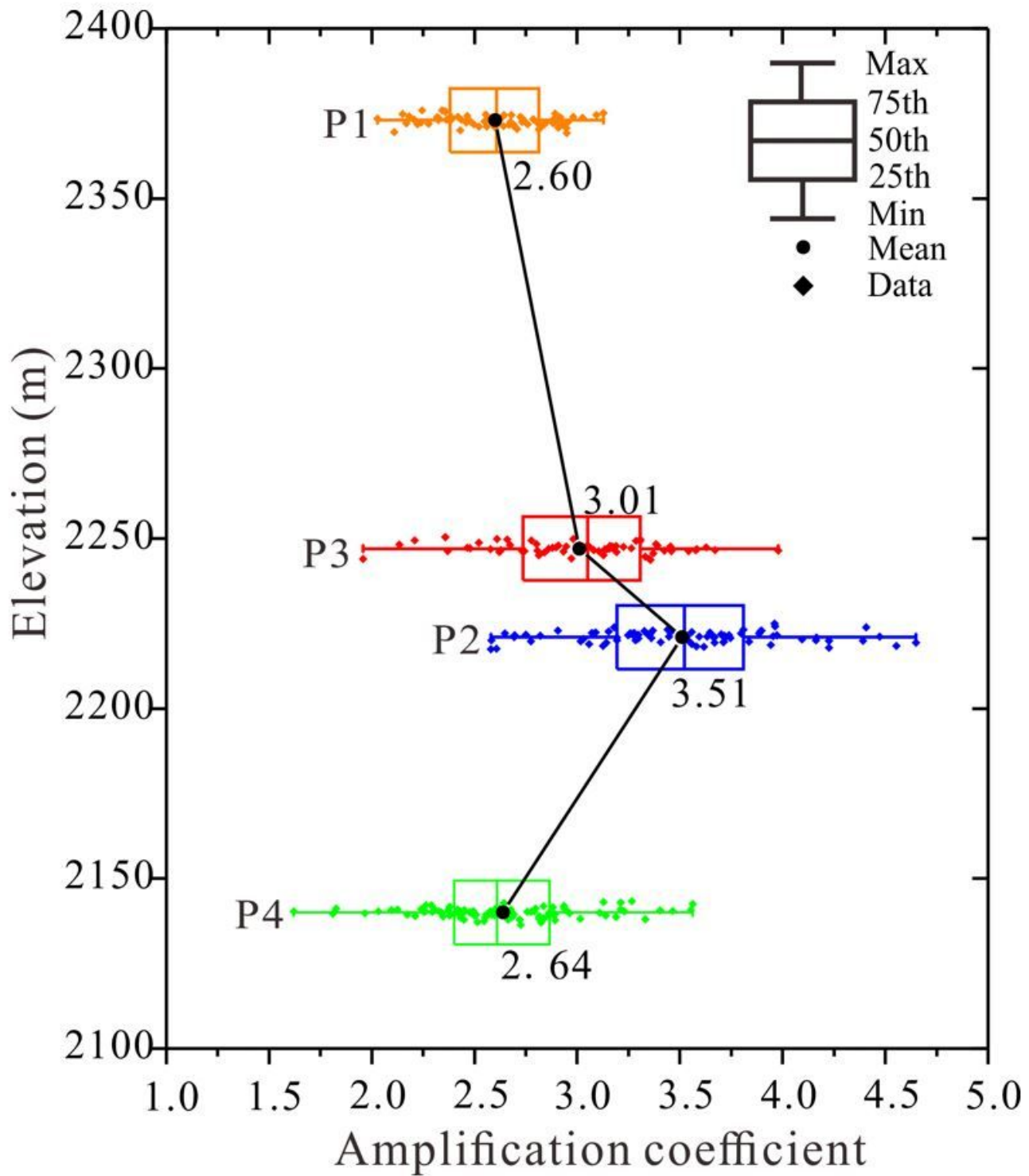


Figure 10

Amplification Coefficients Obtained by HVSR Method

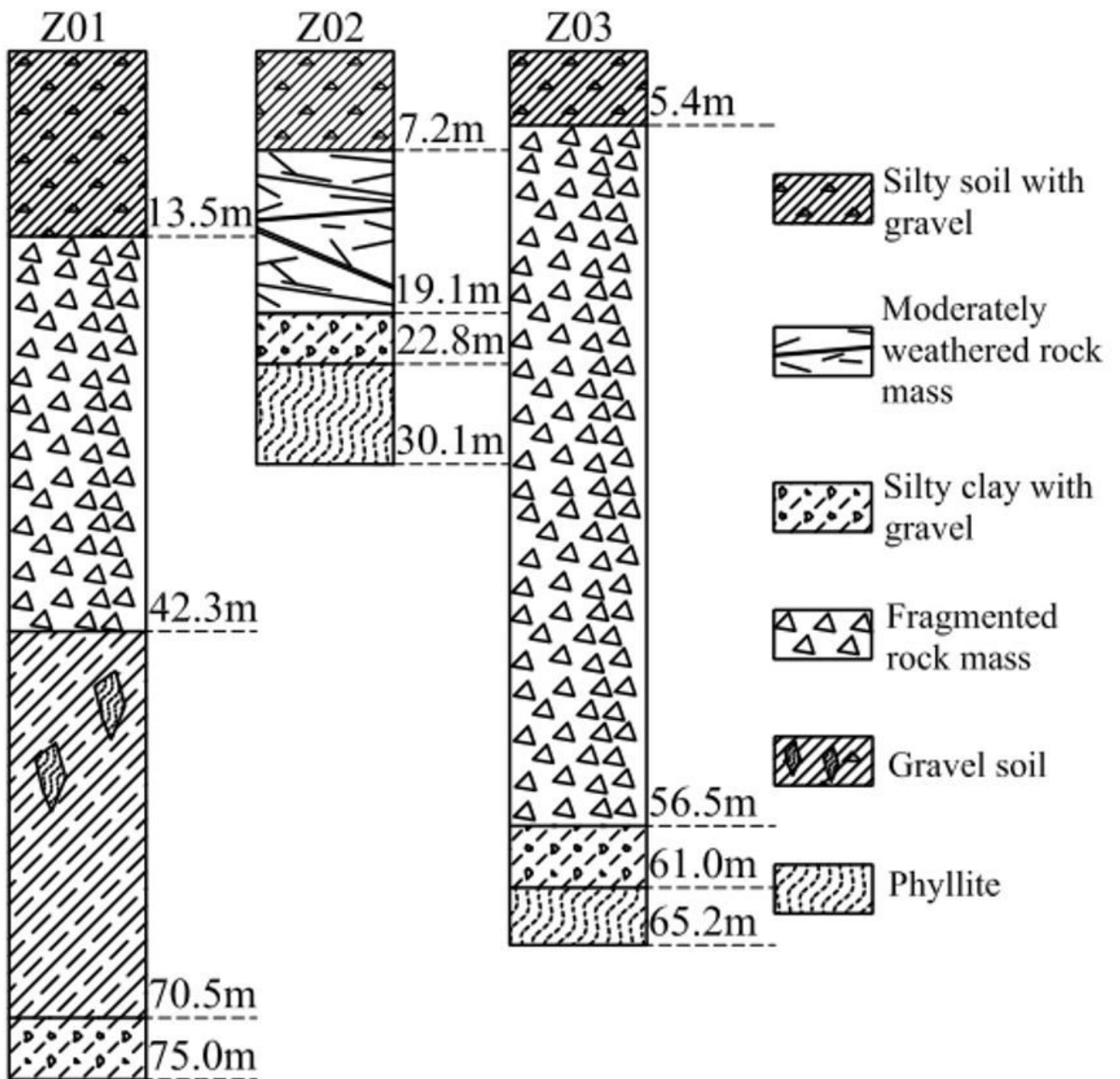


Figure 11

Histogram of Boreholes

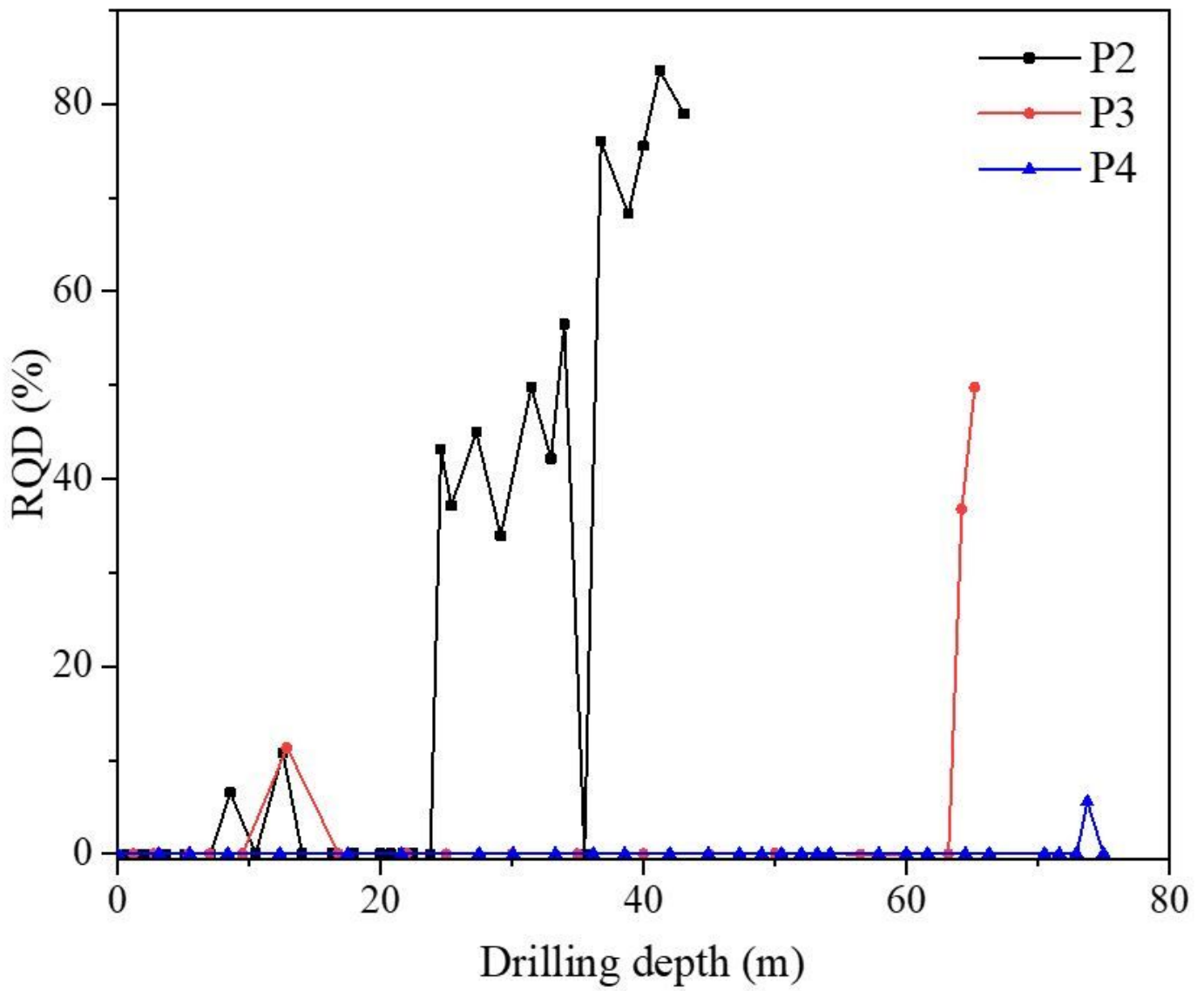
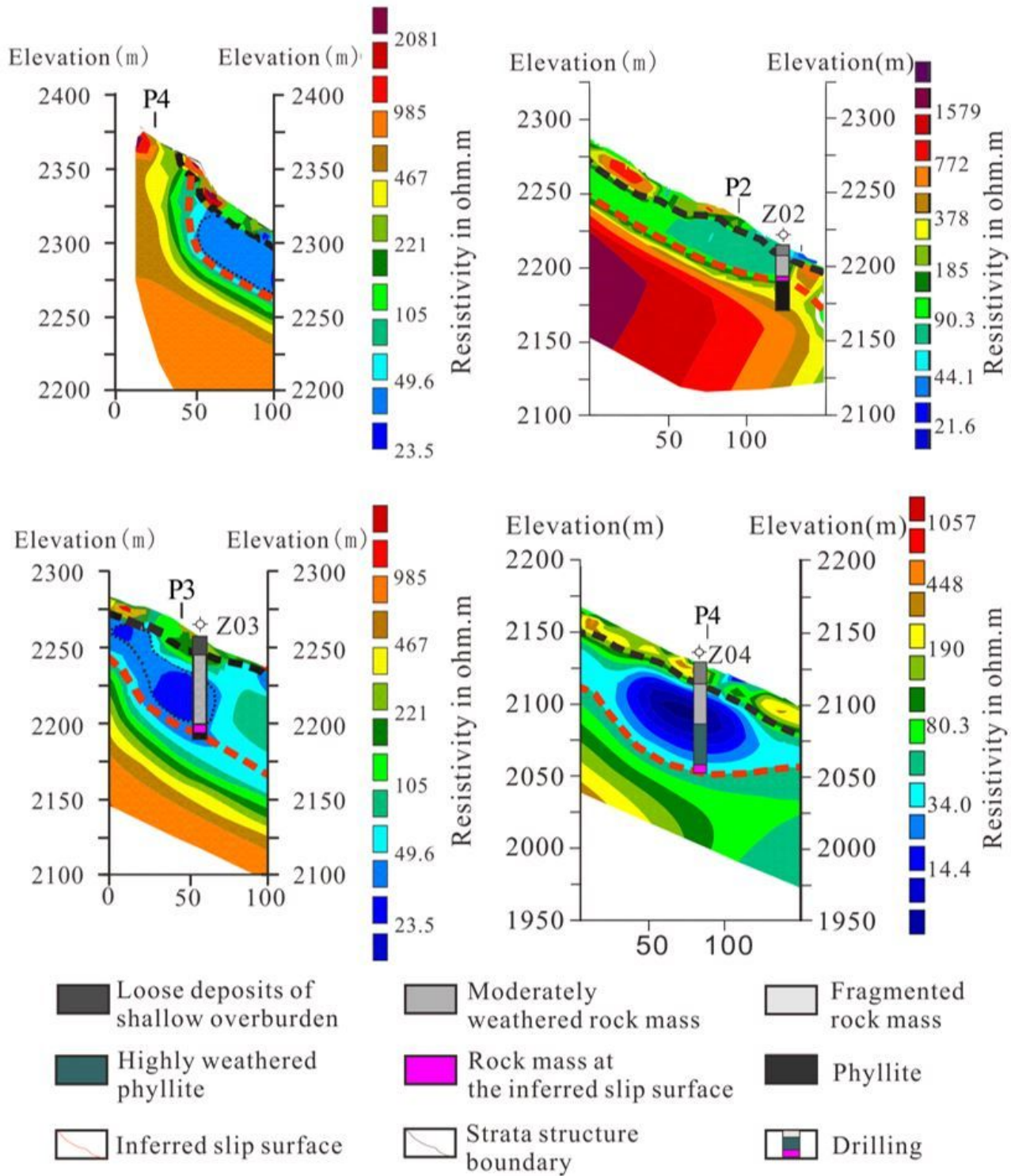


Figure 12

RQD Values of Boreholes at Three Monitoring Stations



**Figure 13**

Resistivity Layout of Underground Structures at Four Monitoring Sites

| Lithofacies                               | Core Picture  | Drilling histogram  | Characteristic                     | RQD (%) | Resistivity (Ohm.m) | Depth (m) |
|---|---|---|------------------------------------|---------|---------------------|-----------|
| 1: Loose deposits of shallow overburden   |    |    | Silty soil with gravel, yellow     | 0       |                     | 5~14      |
| 2: Moderately weathered rock mass         |    |    | A little broken, gray-black        | 0-50    | 50-100              | 7-20      |
| 3: Fragmented rock mass                   |    |    | Extremely broken, less mud content | 0       | 10-50               | 5-60      |
| 4: Highly weathered phyllite              |   |   | Silty clay, gray-black             | 0       | 10-50               | 40-70     |
| 5: Rock mass at the inferred slip surface |  |  | Silty clay with gravel and mud     | 0       | 10-50               | 20-75     |
| 6: Phyllite                               |  |  | gray-black                         | 50-90   | > 100               | 20-80     |

Figure 14

Lithofacies Characteristics, RQD, and Apparent Resistivity